

# Electrical manipulation of antiferromagnetic easy axis in IrMn/NiFe exchange-biased structures

**Jaimin Kang**

Korea Advanced Institute of Science and Technology

**Jeongchun Ryu**

Korea Advanced Institute of Science and Technology

**Jong-Guk Choi**

Korea Advanced Institute of Science and Technology

**Taekhyeon Lee**

Korea Advanced Institute of Science and Technology

**Jaehyeon Park**

Korea Advanced Institute of Science and Technology

**Soogil Lee**

Korea Advanced Institute of Science and Technology <https://orcid.org/0000-0002-8142-3616>

**Kab-Jin Kim**

Korea Advanced Institute of Science and Technology <https://orcid.org/0000-0002-8378-3746>

**Byong-Guk Park** (✉ [bgpark@kaist.ac.kr](mailto:bgpark@kaist.ac.kr))

Korea Advanced Institute of Science and Technology <https://orcid.org/0000-0001-8813-7025>

---

## Article

**Keywords:** Antiferromagnets (AFM), spin-orbit torque (SOT)

**Posted Date:** February 10th, 2021

**DOI:** <https://doi.org/10.21203/rs.3.rs-148179/v1>

**License:**   This work is licensed under a Creative Commons Attribution 4.0 International License.

[Read Full License](#)

---

**Version of Record:** A version of this preprint was published at Nature Communications on November 5th, 2021. See the published version at <https://doi.org/10.1038/s41467-021-26678-x>.

# **Electrical manipulation of antiferromagnetic easy axis in IrMn/NiFe exchange-biased structures**

Jaimin Kang<sup>1</sup>, Jeongchun Ryu<sup>1,\*</sup>, Jong-Guk Choi<sup>1</sup>, Taekhyeon Lee<sup>2</sup>, Jaehyeon Park<sup>2</sup>, Soogil Lee<sup>1</sup>, Kab-Jin Kim<sup>2</sup>, and Byong-Guk Park<sup>1,\*</sup>

<sup>1</sup>*Department of Materials Science and Engineering and KI for Nanocentury, KAIST, Daejeon 34141, Korea*

<sup>2</sup>*Department of Physics, KAIST, Daejeon 34141, Korea*

\* Corresponding authors: Jeongchun Ryu ([jcryu@kaist.ac.kr](mailto:jcryu@kaist.ac.kr)) & Byong-Guk Park ([bgpark@kaist.ac.kr](mailto:bgpark@kaist.ac.kr))

**Electrical control of antiferromagnetic moment is a key technology of antiferromagnet-based spintronics, which promises favourable device characteristics of ultrafast operation and high-density integration compared to conventional ferromagnet-based devices. To date, the manipulation of antiferromagnetic moments has been demonstrated in epitaxial antiferromagnets with broken inversion symmetry or antiferromagnets interfaced with a heavy metal, in which spin-orbit torque (SOT) drives the antiferromagnetic domain wall. Here, we report electrical manipulation of the antiferromagnetic easy axis in IrMn/NiFe bilayers without a heavy metal. We show that the direction of the antiferromagnetic easy axis and associated exchange**

**bias is gradually modulated between up to  $\pm 22$  degrees by in-plane current, which is independent of the NiFe thickness, however. This suggests that spin currents arising in the IrMn layer exert SOTs on uncompensated antiferromagnetic moments at the interface and then rotate the antiferromagnetic moments coherently. Furthermore, the memristive features are preserved in sub-micron devices, facilitating nanoscale multi-level antiferromagnetic spintronic devices.**

Antiferromagnets (AFM), magnetically ordered materials with neighbouring magnetic moments pointing in opposite directions, exhibit the absence of macroscopic magnetization and robustness against external magnetic fields. This, together with their terahertz spin dynamics, promises the development of AFM-based spintronic devices with high-density integration and ultrafast operation that can transcend the capabilities of existing ferromagnet-based spintronic devices<sup>1-8</sup>. On the other hand, the negligible net magnetization makes it difficult to control AFM moments with magnetic fields. Therefore, finding efficient manipulation techniques of AFM order, preferably by electrical means, is of critical importance to realize AFM-based spintronic devices.

The electrical manipulation of AFM moments has been demonstrated in previous reports and can be divided into two categories. The first is to employ a single AFM layer with spatial broken inversion symmetry such as CuMnAs<sup>9-11</sup> or Mn<sub>2</sub>Au<sup>12-15</sup>. In these materials, electric currents locally induce non-equilibrium spin polarization, generating Néel spin-orbit torque (SOT) with opposite signs for each sub-lattice with opposite magnetic moments<sup>16</sup>. However, the Néel SOT demands a specific crystal symmetry, in

which magnetic atoms occupy non-centrosymmetric lattices to form space inversion partners; thus, highly ordered films are required<sup>9–18</sup>. The second is to use AFM/heavy metal bilayers, in which the AFM moment is controlled by the spin current generated by the spin Hall effect<sup>19</sup> in the heavy metal layer and the Rashba-Edelstein effect<sup>20,21</sup> at the interfaces. This is similar to intensively investigated SOT in ferromagnet/heavy metal bilayers<sup>22–25</sup>. Wide ranges of AFMs are explored in the bilayer structures, including metallic AFMs of IrMn<sup>26–30</sup>, PtMn<sup>31,32</sup>, and MnN<sup>33</sup>, an insulating AFM of NiO<sup>34–37</sup>, and a Weyl semimetal AFM of Mn<sub>3</sub>Sn<sup>38</sup>.

Notably, AFM switching typically shows multi-level characteristics<sup>17,31</sup>; the (transverse) resistance of an AFM sample, representing the AFM moment direction, is gradually modulated by the magnitude and polarity of a writing current. This, however, relies on the AFM domain structure because the current-induced SOT controls the overall AFM moments by switching the AFM moment in some domains and/or by driving the AFM domain wall<sup>10,28,32,39</sup>. Therefore, to maintain the memristive behaviour in nano-devices, it is necessary to either engineer an AFM with nanometre-sized domains or find a way to control the AFM moment coherently.

In this article, we report electrical manipulation of the AFM easy axis in exchange-biased IrMn/NiFe bilayer structures. We observe that the planar Hall resistance of the bilayer is gradually modulated by an in-plane current and retains its value even after turning off the current. This demonstrates that the SOT caused by the spin Hall effect in IrMn effectively controls the AFM easy axis and the associated exchange bias between up to  $\pm 22$

degrees. To understand the switching mechanism, we investigate the dependence of the rotation angle of the AFM easy axis ( $\varphi_{\text{AFM}}$ ) on the IrMn and NiFe thicknesses;  $\varphi_{\text{AFM}}$  diminishes with an increase in the IrMn thickness, indicating that the SOT-induced rotation of the AFM easy axis is hindered by the AFM anisotropy, which increases with its thickness. Interestingly,  $\varphi_{\text{AFM}}$  remains constant regardless of the NiFe thickness. This implies that the SOT is not applied directly to the ferromagnetic NiFe layer. Instead, it is applied to uncompensated AFM moments at the IrMn/NiFe interface, subsequently triggering the coherent rotation of the magnetization of the exchange-coupled IrMn/NiFe bilayers. Furthermore, we show that the reversible memristive features of the SOT-induced AFM switching are maintained in a 500-nm-sized device, offering a route for developing nanoscale AFM spintronics devices for neuromorphic computing.

## Results

**Electrical manipulation of the AFM easy axis in IrMn/NiFe.** To demonstrate electrical control of the AFM easy axis, we employ IrMn/NiFe exchange-biased bilayers. In such structures, a charge current induces a spin current through the spin Hall effect in the IrMn layer, exerting torques on the magnetization of the exchange-coupled IrMn/NiFe bilayer. Note that IrMn, a widely used AFM material for exchange bias, exhibits a sizeable (inverse) spin Hall effect<sup>40–44</sup>. As schematically illustrated in Fig. 1a, when applying a charge current in the  $x$ -direction, a spin current flowing in the  $z$ -direction has spin polarization  $\sigma$  in the  $y$ -direction, thus causing the AFM/FM magnetic moment to rotate in a

direction parallel to  $\sigma$ . We fabricate an IrMn (5 nm)/NiFe (4 nm) layer by deposition and subsequent annealing under a magnetic field along the  $x$ -direction to induce an unidirectional exchange-bias field ( $B_{EB}$ ). Figure 1b shows the magnetization curves of the sample while sweeping the magnetic fields in the  $x$ - (blue squares) and  $y$ - (red circles) directions. The hysteresis loop shifts toward the negative field direction only for the measurement along the  $x$ -direction, demonstrating exchange bias developed in the IrMn (5 nm)/NiFe (4 nm) bilayer along the positive  $x$ -direction. The samples are then patterned into a 4- $\mu\text{m}$ -wide Hall bar structure for electrical measurements. First, we measure the planar Hall resistance ( $R_H$ ) of the IrMn/NiFe bilayer while rotating the sample on the  $x$ - $y$  plane under a magnetic field of 100 mT, which is sufficient to saturate the magnetization. Figure 1c shows the  $R_H$  as a function of the azimuthal angle of the magnetic field  $\varphi_B$ , which allows us to extract the magnetization direction of the IrMn/NiFe bilayer  $\varphi_m$  from the measured  $R_H$  value.

We next present the main result of this work; the manipulation of the AFM easy axis through the in-plane current-induced SOT in the IrMn/NiFe structure. Figure 1d shows the changes in  $R_H$  of the IrMn/NiFe bilayer as a function of the in-plane current pulse  $I_P$  with a width of 30  $\mu\text{s}$ . For each  $I_P$ ,  $R_H$  is measured with a reading current of 100  $\mu\text{A}$  after applying  $I_P$ . Initially, the magnetization direction is in the  $x$ -direction ( $\varphi_m = 0^\circ$ ), and the corresponding  $R_H$  value is set to zero by removing an offset. As  $I_P$  increases positively (solid red symbols),  $R_H$  remains unchanged until  $I_P = 15$  mA and gradually increases when  $I_P$  exceeds 15 mA. Finally, for  $I_P = \sim 30$  mA, the  $R_H$  value saturates to -0.14  $\Omega$ , which

corresponds to  $\varphi_m = -15^\circ$ . We observe similar behaviour of the  $R_H$  and the corresponding  $\varphi_m$  but opposite signs when a negative  $I_P$  is applied (solid blue symbols). This demonstrates that the magnetization of the IrMn/NiFe structure is rotated clockwise (counterclockwise) by a positive (negative) in-plane current. Moreover, when we sweep  $I_P$  between  $\pm 33$  mA (open red/blue symbols), the  $R_H$  value varies between  $\mp 0.14 \Omega$ , demonstrating the electrical modulation of  $\varphi_m$  of  $\mp 15^\circ$  in a reversible manner.

We further investigate whether the change in the  $R_H$  value manifests the rotation of the AFM easy axis of IrMn, given that the  $R_H$  value of the IrMn/NiFe bilayer is mostly dominated by NiFe. To this end, we measure the dependence of  $R_H$  on the magnetic field along the  $x$ -direction  $B_x$ . Prior to the measurement, we apply an  $I_P$  of -30 mA to set  $R_H = 0.14 \Omega$  (or  $\varphi_m = +15^\circ$ ). Figure 1e shows that  $R_H$  gradually decreases with an increase in  $B_x$  (red squares) and approaches zero when  $B_x = 200$  mT. This indicates that the magnetization rotates towards the magnetic field direction as expected. Interestingly, when reducing  $B_x$ ,  $R_H$  is restored to its initial value (red line in Fig. 1e); i.e., the magnetization rotates back to  $+15^\circ$ , as depicted in the inset of Fig. 1e. The same behaviour is observed when  $R_H$  is initialized to  $-0.14 \Omega$  (blue squares and line in Fig. 1e). The spontaneous recovery of  $R_H$  (or  $\varphi_m$ ) indicates that there is a bias field acting on NiFe in the direction of  $\varphi = \pm 15^\circ$ , which we attribute to the exchange bias originating from the AFM IrMn. This result provides evidence that the AFM easy axis  $\varphi_{AFM}$  ( $//\varphi_m$ ) is electrically manipulated in an IrMn/NiFe bilayer structure via the current-induced SOT. Note that the changes in  $R_H$  with  $I_P$  are not observed in a Ta/NiFe sample, in which spin current is effectively generated by the spin

Hall effect in Ta<sup>45,46</sup>, though. In the structure without an AFM layer, the magnetization rotated by the SOT returns to its easy axis (that is in the  $x$ -direction) once the current is turned off, resulting in no variation of  $R_H$  and  $\varphi_m$  (Supplementary Figure S1). This again confirms that AFM IrMn plays a critical role in the electrical modulation of  $\varphi_m$  in the IrMn/NiFe structure.

**Mechanisms of SOT-induced AFM switching.** To understand the underlying mechanism of the electrical manipulation of the AFM easy axis, we investigate various IrMn/NiFe structures. Assuming that the spin current is only generated in the IrMn layer, there are two possible scenarios; first, the spin current exerts torques on entire AFM moments, similar to the Néel SOT in CuMnAs<sup>9,16</sup>, although this phenomenon is expected to be absent in polycrystalline IrMn layers. Second, the spin current induces spin accumulation on the IrMn/NiFe interface, giving torques to NiFe and controlling its magnetization. This is followed by the rotation of the exchange-coupled IrMn moment. In the latter case, where opposite spins are accumulated on the top and bottom interfaces, the rotation direction will reverse when changing the stacking order, whereas it is independent of the stacking order in the former case. To verify this, we measure the  $R_H$  versus  $I_P$  curves using a NiFe (4 nm)/IrMn (5 nm) sample, an inverted structure of the IrMn/NiFe, which is shown in Fig. 1d. Figure 2a shows that the  $\varphi_{AFM}$  extracted from the  $R_H$  value rotates reversibly within  $\pm 15^\circ$  by the in-plane current, but its polarity is reversed. This indicates that the spin current in the IrMn and associated spin accumulation at the IrMn/NiFe interface are primarily responsible

for the electrical manipulation of the magnetization of IrMn/NiFe bilayers. We note that the sample temperature increases due to the current injection, which may reduce the AFM anisotropy and thereby assists the rotation of the AFM moment. Furthermore, to rule out the possible effects of Oersted fields generated by a current flowing into the IrMn layer, we examine an IrMn (5 nm)/NiFe (4 nm)/Ta (1.5 nm) structure, where the Ta layer diminishes the Oersted field effect, but it provides additional spin currents injected into NiFe layer since Ta has a negative spin Hall angle opposite to IrMn<sup>40,43</sup>. Figure 2b shows the results; by introducing the Ta layer, the current-induced variation of  $\varphi_{\text{AFM}}$  is enhanced to  $\pm 22^\circ$  while switching polarity remains the same. This indicates that the Oersted field contribution is not significant in this measurement, accentuating that the spin current in IrMn and the associated SOT is the main cause of the electrical manipulation of the AFM moment.

We subsequently study the thickness dependence of the SOT-induced manipulation of the AFM easy axis. Figure 3a shows the hysteresis loops of the IrMn ( $t_{\text{IrMn}}$ )/NiFe (4 nm) bilayers, where the IrMn thickness ( $t_{\text{IrMn}}$ ) ranges from 5 to 25 nm, demonstrating that the exchange bias field ( $B_{\text{EB}}$ ) increases with an increase in  $t_{\text{IrMn}}$ . This is attributed to the enhancement of the AFM anisotropy for a thicker  $t_{\text{IrMn}}$ <sup>47,48</sup>. Figure 3b plots the  $\varphi_{\text{AFM}}$  versus current density  $J_{\text{P}}$  curves for samples with different  $t_{\text{IrMn}}$ ; the maximum value of  $\varphi_{\text{AFM}}$  achieved by SOT is gradually reduced as  $t_{\text{IrMn}}$  is increased (See Supplementary Figure S2 for the full set of data). Figure 3c summarizes the results showing that the maximum variation of the  $\varphi_{\text{AFM}}$  value [ $\Delta\varphi_{\text{AFM}} = \varphi_{\text{AFM}}(-I) - \varphi_{\text{AFM}}(+I)$ ] is inversely proportional to the magnitude of  $B_{\text{EB}}$ . This indicates that the SOT-induced rotation of the AFM easy axis is

impeded by the AFM anisotropy developed in the  $x$ -direction. Therefore,  $\varphi_{\text{AFM}}$  can be further enhanced by reducing the AFM anisotropy as long as the exchange-coupling with FM is preserved.

We also examine the dependence of  $B_{\text{EB}}$  and  $\varphi_{\text{AFM}}$  on the NiFe thickness ( $t_{\text{NiFe}}$ ) in IrMn (5 nm)/NiFe ( $t_{\text{NiFe}}$ ) bilayers, where  $t_{\text{NiFe}}$  is varied from 3 to 10 nm. Figure 3d and e show the hysteresis loops and the  $\varphi_{\text{AFM}}$  versus  $J_{\text{P}}$  curves of the samples, respectively (See Supplementary Figure S2 for the full set of data). As summarized in Fig. 3f,  $B_{\text{EB}}$  remains unchanged for  $t_{\text{NiFe}}$ 's up to 7 nm and decreases slightly for a  $t_{\text{NiFe}}$  of 10 nm, which is the general trend of the reduction of  $B_{\text{EB}}$  for thicker FMs<sup>47,49</sup>. Interestingly,  $\Delta\varphi_{\text{AFM}}$  exhibits  $\sim 30^\circ$  for all samples regardless of  $t_{\text{NiFe}}$ 's used in this study. This is inconsistent with the aforementioned assumption that spin currents generated in IrMn exert SOTs on NiFe, in which case the magnitude of SOT (or the maximum  $\varphi_{\text{AFM}}$  value) should decrease with an increase in  $t_{\text{NiFe}}$  because spin currents are mostly absorbed at the FM interface when injected into an FM layer. This result suggests that the SOT-induced AFM switching is an interface phenomenon; therefore, we infer that the spin current gives spin torques to the interfacial uncompensated AFM moments, rotating the magnetization directions of the exchange-coupled IrMn and NiFe simultaneously.

**Memristive behaviour of AFM switching.** We finally discuss memristive characteristics based on SOT-induced AFM switching in a reversible and non-volatile manner. Figure 4a shows minor  $\varphi_{\text{AFM}} - I_{\text{P}}$  curves of the IrMn (5 nm)/NiFe (4 nm)/Ta (1.5 nm) structure with a

4- $\mu\text{m}$ -wide Hall bar. As shown in the measurement sequence illustrated in Fig. 4b, we first apply an initializing current pulse  $I_{P,\text{ini}}$  of -32 mA to set  $\varphi_{\text{AFM}} = +22^\circ$  and then measure  $R_{\text{H}}$  while sweeping  $I_{\text{P}}$  between -32 mA and the positive maximum  $I_{\text{P}} [I_{\text{P}(+\text{max})}]$ . The measurement is repeated as we increase  $I_{\text{P}(+\text{max})}$  from +22 mA to +31 mA. This result demonstrates that multiple  $\varphi_{\text{AFM}}$  values between  $\pm 22^\circ$  can be obtained according to the magnitude of  $I_{\text{P}(+\text{max})}$ . Similar results of minor loops are observed when sweeping  $I_{\text{P}}$  between +32 mA and the negative maximum  $I_{\text{P}}$  (Supplementary Figure S3). We test whether the memristive feature is maintained in nanoscale devices. Figure 4c shows the minor  $\varphi_{\text{AFM}} - I_{\text{P}}$  curves of the IrMn (5 nm)/NiFe (5 nm) structure with a 500-nm-wide Hall bar, as measured with experimental procedures similar to that shown in Fig. 4a,b. Multi-level  $\varphi_{\text{AFM}}$  values are successfully achieved in the 500 nm device, comparable to those in the 4  $\mu\text{m}$  sample. This implies that the gradual change of  $\varphi_{\text{AFM}}$  in IrMn/NiFe bilayers is due to the collective rotation of the AFM easy axis and the exchange-coupled FM moment, which is distinct from the previous results based on AFM domain wall motions<sup>28,29,39,50</sup>. The scalable memristive characteristics can facilitate electrically controlled multi-level spintronic devices for neuromorphic computing.

## Discussion

We have demonstrated reversible electrical manipulation of the AFM easy axis in IrMn/NiFe exchange-biased structures. We observe that the SOT caused by the spin Hall effect in IrMn effectively controls the AFM easy axis and the associated exchange bias

between up to  $\pm 22$  degrees. The maximum rotation angle of the AFM easy axis achieved by SOT is independent of the NiFe thicknesses, indicating a critical role of interfacial uncompensated AFM moments that mediates the spin torque to the entire AFM and exchange-coupled FM moments. Moreover, the memristive behaviour, the gradual manipulation of the AFM easy axis according to the polarity and amplitude of the electric current, can be observed in a 500 nm device. Our results demonstrating the electrical control of the AFM moment in a reversible and non-volatile manner paves the way for the realization of nanoscale AFM-based spintronics for neuromorphic applications.

## Methods

**Sample preparation.** Samples of IrMn/NiFe, IrMn/NiFe/Ta, NiFe/IrMn, and Ta/NiFe structures were deposited on high-resistive Si substrates using ultrahigh-vacuum magnetron sputtering with a base pressure of less than  $4.0 \times 10^{-6}$  Pa. During the sputtering process, a magnetic field of 15 mT was applied to induce uniaxial anisotropy. A capping layer of MgO (3.2 nm)/Ta (2 nm) was used to protect samples from oxidation. The metal layers were grown by DC sputtering (30W) with a working pressure of 0.4 Pa, while the MgO layer was deposited by RF sputtering (150W) at 1.33 Pa. After the deposition step, the samples were annealed at 200 °C for 40 minutes in a vacuum with a magnetic field of 100 mT to develop exchange bias. The magnetic hysteresis loop was measured using vibrating sample magnetometer. For the electrical measurements, a Hall bar structure with a 4  $\mu\text{m}$  (or 500 nm) width was patterned by photo- (or e-beam-) lithography and Ar ion etching. Electrical contacts were formed by the deposition of Ru (50 nm) and a subsequent lift-off process.

**Electrical measurements.** Planar Hall resistance ( $R_H$ ) was measured with a reading current of 100  $\mu\text{A}$  while rotating the samples on the  $x$ - $y$  plane under an external magnetic field of 100 mT. For the current-induced AFM switching measurements,  $R_H$  was measured with a reading current of 100  $\mu\text{A}$  after 500 ms of each current pulse ( $I_P$ ) application of 30  $\mu\text{s}$  width. The constant offset of  $R_H$ , which may be caused by the misalignment of the Hall cross, is removed such that  $R_H = 0$  corresponds to the magnetization aligned to the  $x$ -direction ( $\varphi_m =$

0°). All switching measurements were performed at room temperature without an external magnetic field.

### Data availability

The data that support the findings of this study are available from the corresponding author upon reasonable request.

### References

1. Jungwirth, T., Marti, X., Wadley, P. & Wunderlich, J. Antiferromagnetic spintronics. *Nat. Nanotechnol.* **11**, 231–241 (2016).
2. Park, B.-G. et al. A spin-valve-like magnetoresistance of an antiferromagnet-based tunnel junction. *Nat. Mater.* **10**, 347–351 (2011).
3. Wang, Y. Y. et al. Room-temperature perpendicular exchange coupling and tunneling anisotropic magnetoresistance in an antiferromagnet-based tunnel junction. *Phys. Rev. Lett.* **109**, 137201 (2012).
4. Marti, X. et al. Room-temperature antiferromagnetic memory resistor. *Nat. Mater.* **13**, 367–374 (2014).
5. Baltz, V. et al. Antiferromagnetic spintronics. *Rev. Mod. Phys.* **90**, 15005 (2018).
6. Jungwirth, T. et al. The multiple directions of antiferromagnetic spintronics. *Nat. Phys.* **14**, 200–203 (2018).
7. Olejník, K. et al. Terahertz electrical writing speed in an antiferromagnetic memory. *Sci. Adv.* **4**, eaar3566 (2018).
8. Khymyn, R. et al. Ultra-fast artificial neuron: generation of picosecond-duration spikes in a current-driven antiferromagnetic auto-oscillator. *Sci. Rep.* **8**, 15727 (2018).
9. Wadley, P. et al. Electrical switching of an antiferromagnet. *Science.* **351**, 587–590 (2016).

10. Grzybowski, M. J. et al. Imaging current-induced switching of antiferromagnetic domains in CuMnAs. *Phys. Rev. Lett.* **118**, 57701 (2017).
11. Godinho, J. et al. Electrically induced and detected Néel vector reversal in a collinear antiferromagnet. *Nat. Commun.* **9**, 4686 (2018).
12. Bodnar, S. Y. et al. Writing and reading antiferromagnetic Mn<sub>2</sub>Au by Néel spin-orbit torques and large anisotropic magnetoresistance. *Nat. Commun.* **9**, 348 (2018).
13. Sapozhnik, A. A. et al. Direct imaging of antiferromagnetic domains in Mn<sub>2</sub>Au manipulated by high magnetic fields. *Phys. Rev. B* **97**, 134429 (2018).
14. Meinert, M., Graulich, D. & Matalla-Wagner, T. Electrical switching of antiferromagnetic Mn<sub>2</sub>Au and the role of thermal activation. *Phys. Rev. Appl.* **9**, 64040 (2018).
15. Zhou, X. F. et al. From fieldlike torque to antidamping torque in antiferromagnetic Mn<sub>2</sub>Au. *Phys. Rev. Appl.* **11**, 54030 (2019).
16. Železný, J. et al. Relativistic Néel-order fields induced by electrical current in antiferromagnets. *Phys. Rev. Lett.* **113**, 157201 (2014).
17. Olejník, K. et al. Antiferromagnetic CuMnAs multi-level memory cell with microelectronic compatibility. *Nat. Commun.* **8**, 15434 (2017).
18. Zhou, X. F. et al. Strong orientation-dependent spin-orbit torque in thin films of the antiferromagnet Mn<sub>2</sub>Au. *Phys. Rev. Appl.* **9**, 054028 (2018).
19. Dyakonov, M. & Perel, V. I. Current-induced spin orientation of electrons in semiconductors. *Phys. Lett. A* **35A**, 459–460 (1971).
20. Bychkov, Y. A. & Rashba, E. I. Oscillatory effects and the magnetic susceptibility of carriers in inversion layers. *J. Phys. C Solid State Phys.* **17**, 6039–6045 (1984).
21. Edelstein, V. M. Spin polarization of conduction electrons induced by electric current in two-dimensional asymmetric electron systems. *Solid State Commun.* **73**, 233–235 (1990).
22. Liu, L. et al. Spin-torque switching with the giant spin Hall effect of tantalum. *Science*. **336**, 555–558 (2012).

23. Miron, I. M. et al. Perpendicular switching of a single ferromagnetic layer induced by in-plane current injection. *Nature* **476**, 189–193 (2011).
24. Ryu, J., Lee, S., Lee, K.-J. & Park, B.-G. Current-induced spin-orbit torques for spintronic applications. *Adv. Mater.* **32**, 1907148 (2020).
25. Manchon, A. et al. Current-induced spin-orbit torques in ferromagnetic and antiferromagnetic systems. *Rev. Mod. Phys.* **91**, 35004 (2019).
26. Lin, P.-H. et al. Manipulating exchange bias by spin-orbit torque. *Nat. Mater.* **18**, 335–341 (2019).
27. Kim, H.-J., Je, S.-G., Jung, D.-H., Lee, K.-S. & Hong, J.-Il. Field-free control of exchange bias by spin Hall currents. *Appl. Phys. Lett.* **115**, 022401 (2019).
28. Yun, J. et al. Tailoring multilevel-stable remanence states in exchange-biased system through spin-orbit torque. *Adv. Funct. Mater.* **30**, 1909092 (2020).
29. Liu, X. H., Edmonds, K. W., Zhou, Z. P. & Wang, K. Y. Tuning interfacial spins in antiferromagnetic-ferromagnetic-heavy-metal heterostructures via spin-orbit torque. *Phys. Rev. Appl.* **13**, 14059 (2020).
30. Peng, S. et al. Exchange bias switching in an antiferromagnet/ferromagnet bilayer driven by spin-orbit torque. *Nat. Electron.* (2020) doi:10.1038/s41928-020-00504-6.
31. Shi, J. et al. Electrical manipulation of the magnetic order in antiferromagnetic PtMn pillars. *Nat. Electron.* **3**, 92–98 (2020).
32. DuttaGupta, S. et al. Spin-orbit torque switching of an antiferromagnetic metallic heterostructure. *Nat. Commun.* **11**, 5715 (2020).
33. Dunz, M., Matalla-Wagner, T. & Meinert, M. Spin-orbit torque induced electrical switching of antiferromagnetic MnN. *Phys. Rev. Res.* **2**, 13347 (2020).
34. Moriyama, T., Oda, K., Ohkochi, T., Kimata, M. & Ono, T. Spin torque control of antiferromagnetic moments in NiO. *Sci. Rep.* **8**, 14167 (2018).
35. Fischer, J. et al. Spin Hall magnetoresistance in antiferromagnet/heavy-metal heterostructures. *Phys. Rev. B* **97**, 014417 (2018).

36. Baldrati, L. et al. Full angular dependence of the spin Hall and ordinary magnetoresistance in epitaxial antiferromagnetic NiO(001)/Pt thin films. *Phys. Rev. B* **98**, 24422 (2018).
37. Chen, X. Z. et al. Antidamping-torque-induced switching in biaxial antiferromagnetic insulators. *Phys. Rev. Lett.* **120**, 207204 (2018).
38. Tsai, H. et al. Electrical manipulation of a topological antiferromagnetic state. *Nature* **580**, 608–613 (2020).
39. Kurenkov, A., Zhang, C., DuttaGupta, S., Fukami, S. & Ohno, H. Device-size dependence of field-free spin-orbit torque induced magnetization switching in antiferromagnet/ferromagnet structures. *Appl. Phys. Lett.* **110**, 92410 (2017).
40. Zhang, W. et al. Spin Hall effects in metallic antiferromagnets. *Phys. Rev. Lett.* **113**, 196602 (2014).
41. Mendes, J. B. S. et al. Large inverse spin Hall effect in the antiferromagnetic metal Ir<sub>20</sub>Mn<sub>80</sub>. *Phys. Rev. B* **89**, 140406(R) (2014).
42. Chen, H., Niu, Q. & Macdonald, A. H. Anomalous Hall effect arising from noncollinear antiferromagnetism. *Phys. Rev. Lett.* **112**, 017205 (2014).
43. Oh, Y.-W. et al. Field-free switching of perpendicular magnetization through spin-orbit torque in antiferromagnet/ferromagnet/oxide structures. *Nat. Nanotechnol.* **11**, 878–884 (2016).
44. Fukami, S., Zhang, C., DuttaGupta, S., Kurenkov, A. & Ohno, H. Magnetization switching by spin-orbit torque in an antiferromagnet–ferromagnet bilayer system. *Nat. Mater.* **15**, 535–541 (2016).
45. Garello, K. et al. Symmetry and magnitude of spin-orbit torques in ferromagnetic heterostructures. *Nat. Nanotechnol.* **8**, 587–593 (2013).
46. Kim, J. et al. Layer thickness dependence of the current-induced effective field vector in Ta|CoFeB|MgO. *Nat. Mater.* **12**, 240–245 (2013).
47. Nogués, J. & Schuller, I. K. Exchange bias. *J. Magn. Magn. Mater.* **192**, 203–232 (1999).

48. Kim, D.-J. et al. Utilization of the antiferromagnetic IrMn electrode in spin thermoelectric devices and their beneficial hybrid for thermopiles. *Adv. Funct. Mater.* **26**, 5507–5514 (2016).
49. Lee, J. H. et al. Thermal stability of the exchanged biased CoFe/IrMn electrode for the magnetic tunnel junction as a function of CoFe thickness. *J. Appl. Phys.* **92**, 6241–6244 (2002).
50. Liu, F. & Ross, C. A. Size-dependent magnetic properties of 100–500 nm diameter IrMn/NiFe disks made by a two-step deposition process. *J. Appl. Phys.* **116**, 194307 (2014).

### **Acknowledgments**

This work was supported by the National Research Foundation of Korea (NRF-2015 M3D1A1070465, 2016R1A5A1008184, 2020R1A2C2010309).

### **Author contributions**

B.-G.P. planned and supervised the study. J.K., J.-G.C, and J.R. fabricated devices. J.K. and J.R. performed electrical and magnetic measurements with help from S.L., J.P., T.L., and K.-J.K. All authors discussed the results, and J.K., J.R. and B.-G.P. wrote the manuscript.

### **Competing interests**

The authors declare no competing interests.

**Correspondence and requests for materials** should be addressed to J.R. (jcryu@kaist.ac.kr) and B.-G. P. ([bgpark@kaist.ac.kr](mailto:bgpark@kaist.ac.kr))

## Figures

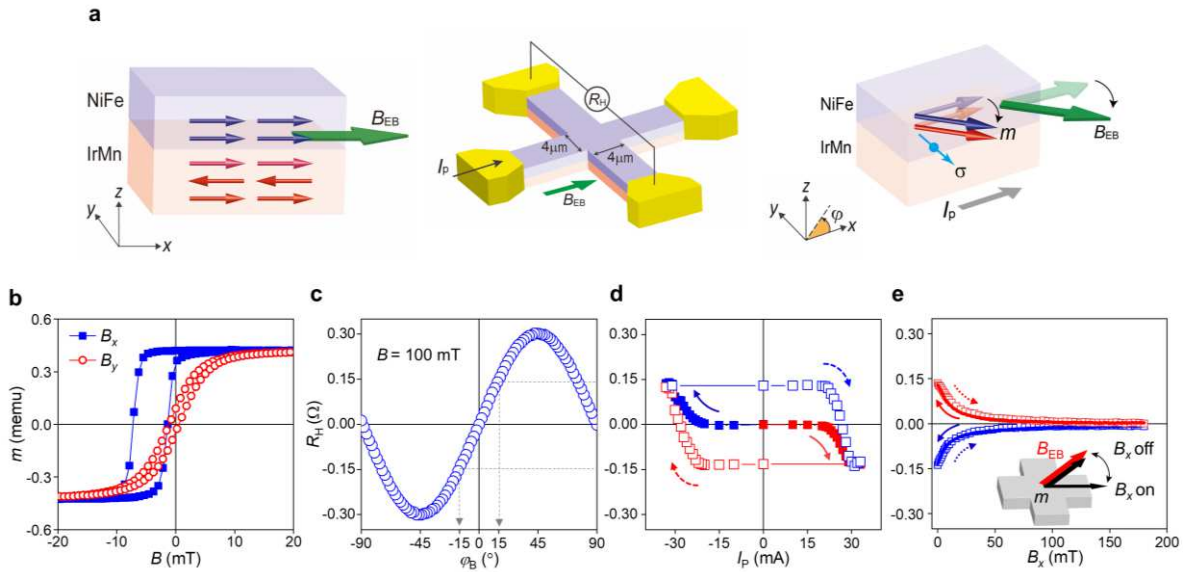


**Figure 1 | Electrical manipulation of the AFM easy axis in IrMn/NiFe structure. a,** Left: Exchange-biased IrMn/NiFe structure, where the blue and red arrows represent magnetization ( $m$ ) of NiFe and IrMn, respectively, and  $B_{EB}$  is the exchange bias field. Middle: The Hall bar device for electrical measurements. The Hall resistance ( $R_H$ ) is measured after applying an in-plane current pulse  $I_P$ . Right: Schematics of the current-induced AFM switching, where the magnetization direction of the IrMn/NiFe bilayer ( $\varphi_m$ ) is modulated by the spin current with spin polarization ( $\sigma$ ). **b,** Hysteresis loop of IrMn (5 nm)/NiFe (4 nm) structure measured with magnetic fields along the  $x$ -axis (solid blue) and  $y$ -axis (open red). **c,**  $R_H$  versus azimuthal angle of a magnetic field ( $\varphi_B$ ) of 100 mT. **d,** The  $R_H$  vs  $I_P$  curves, where the arrows denote the sweeping direction of  $I_P$ . **e,**  $R_H$  as a function of a magnetic field along  $x$ -axis ( $B_x$ ).  $R_H$  is initially set to  $\pm 0.14$  by an  $I_P$  of  $\mp 30$  mA, represented by the red and blue symbols. Open squares (lines) refer to increasing (decreasing)  $B_x$ . The inset illustrates the magnetization changes by  $B_x$ .

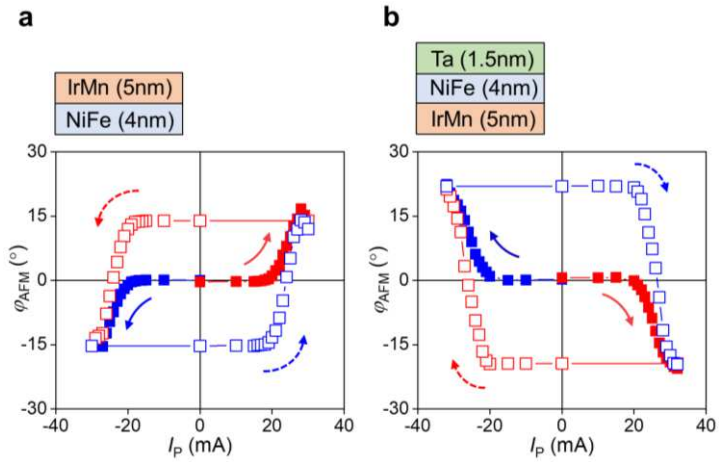


**Figure 2 | SOT-induced AFM switching for various IrMn/NiFe structures. a, b,** AFM easy axis ( $\varphi_{AFM}$ ) versus  $I_P$  curves for the NiFe (4 nm)/IrMn (5 nm) sample (**a**) and the IrMn (5 nm)/NiFe (4 nm)/Ta (1.5 nm) sample (**b**). The arrows denote the sweeping direction of  $I_P$ . The  $\varphi_{AFM}$  values are extracted from the  $R_H$  values.

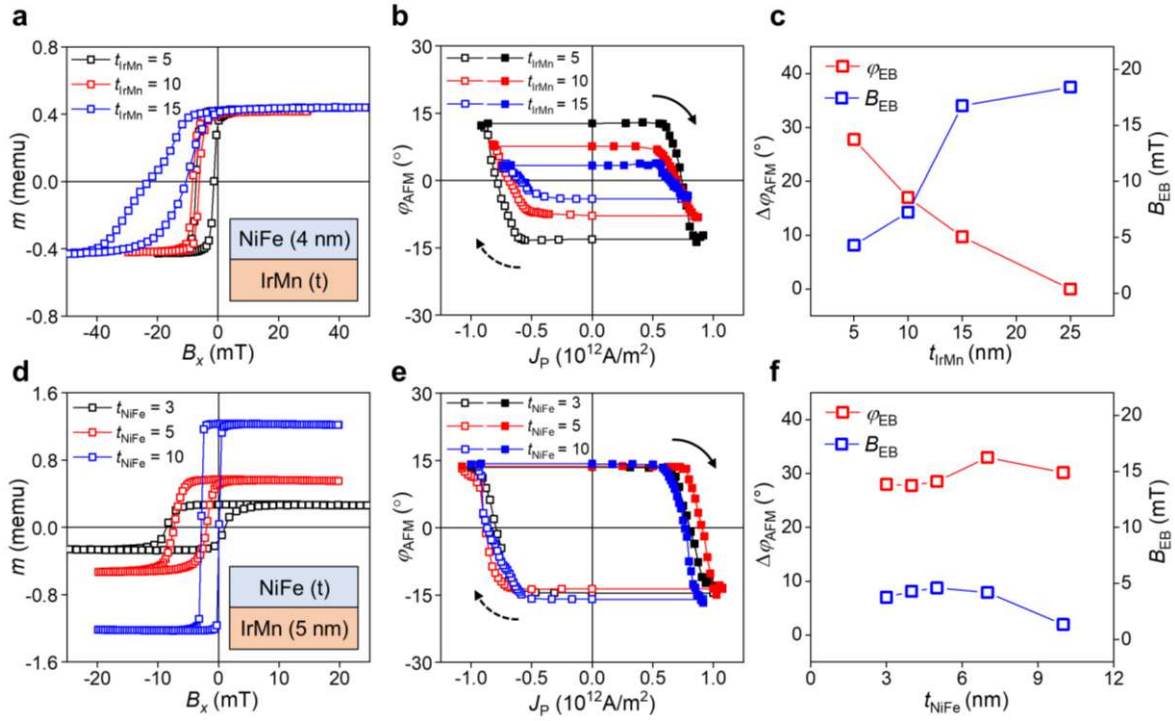


**Figure 3 | Thickness dependence of SOT-induced AFM switching.** **a-c.** Hysteresis loop measured using a magnetic field along the  $x$ -axis,  $B_x$  (**a**), The  $\varphi_{\text{AFM}}$  versus current density ( $J_P$ ) curves, where the arrows denote the sweeping direction of  $J_P$  (**b**),  $\Delta\varphi_{\text{AFM}} [= \varphi_{\text{AFM}}(-I) - \varphi_{\text{AFM}}(+I)]$  and  $B_{\text{EB}}$  as a function of IrMn thickness  $t_{\text{IrMn}}$  (**c**) of the IrMn ( $t_{\text{IrMn}}$ )/NiFe (4 nm) samples with different  $t_{\text{IrMn}}$ 's ranging from 5 to 25 nm. **d-f.** Hysteresis loop measured using  $B_x$  (**d**), The  $\varphi_{\text{AFM}}$  versus  $J_P$  curves, where the arrows denote the sweeping direction of  $J_P$  (**e**), The  $\Delta\varphi_{\text{AFM}}$  and  $B_{\text{EB}}$  versus  $t_{\text{NiFe}}$  (**f**) of the IrMn (5 nm)/NiFe ( $t_{\text{NiFe}}$ ) samples with different  $t_{\text{NiFe}}$ 's ranging from 3 to 10 nm.

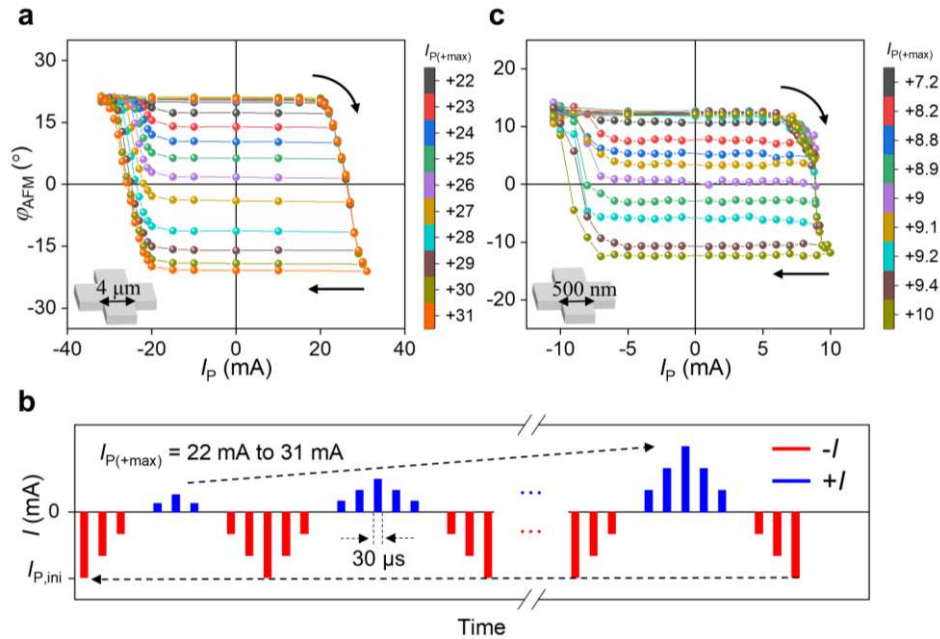


**Figure 4 | Memristive behaviour of AFM switching.** **a**, Minor  $\varphi_{AFM}$  vs  $I_P$  curves for the IrMn (5 nm)/NiFe (4 nm)/Ta (1.5 nm) sample with a 4- $\mu\text{m}$ -wide Hall bar. The arrows denote the sweeping direction of  $I_P$ , **b**, Schematics of the measurement sequence;  $I_{P,ini}$  is the initializing current pulse of -32 mA and  $I_{P(+max)}$  is the positive maximum  $I_P$ . Minor loops are consecutively measured while sweeping  $I_P$  between -32 mA and  $I_{P(+max)}$ , which increases from +22 mA to +31 mA. **c**, Minor  $\varphi_{AFM}$  vs  $I_P$  curves for the IrMn (5 nm)/NiFe (5 nm) sample with a 500-nm-wide Hall bar. The arrows denote the sweeping direction of  $I_P$ .

# Figures

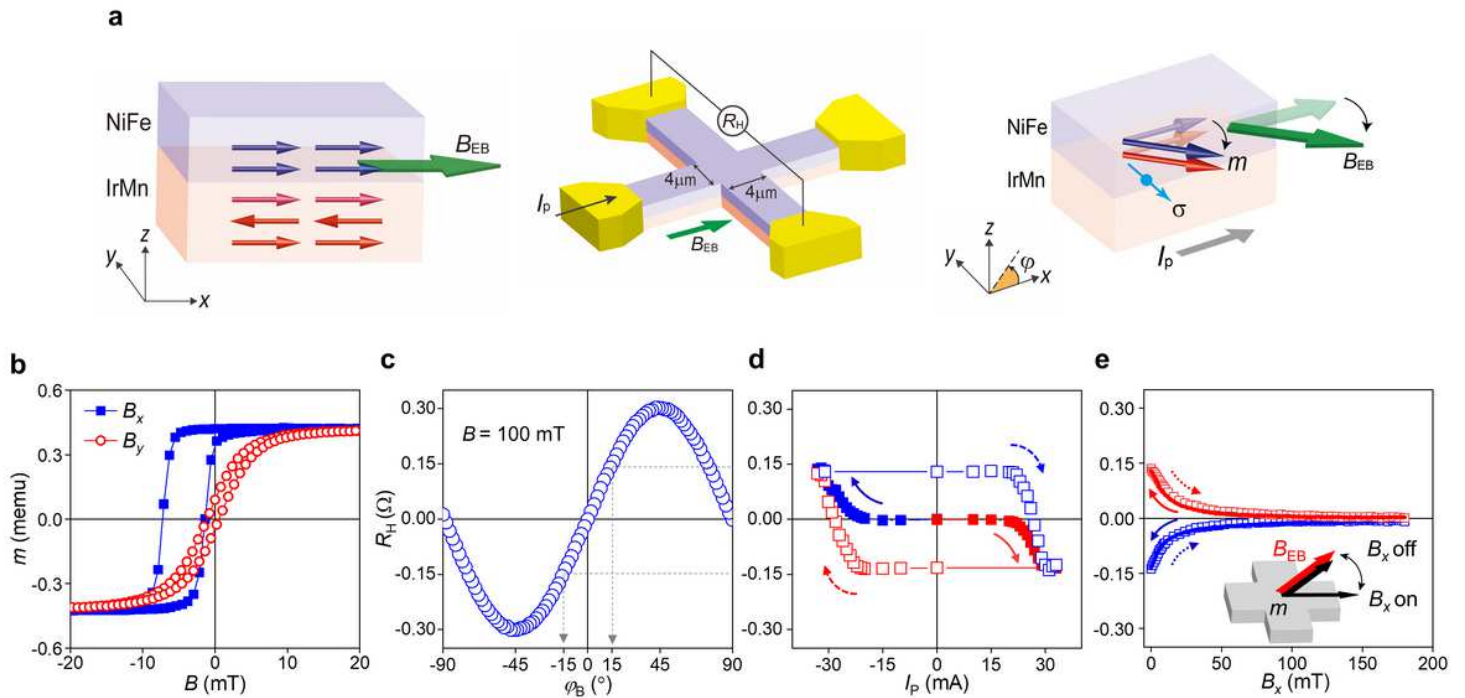


**Figure 1**

Electrical manipulation of the AFM easy axis in IrMn/NiFe structure. a, Left: Exchange-biased IrMn/NiFe structure, where the blue and red arrows represent magnetization ( $m$ ) of NiFe and IrMn, respectively, and  $B_{EB}$  is the exchange bias field. Middle: The Hall bar device for electrical measurements. The Hall resistance ( $R_H$ ) is measured after applying an in-plane current pulse  $I_p$ . Right: Schematics of the current-induced AFM switching, where the magnetization direction of the IrMn/NiFe bilayer ( $\phi_m$ ) is modulated by the spin current with spin polarization ( $s$ ). b, Hysteresis loop of IrMn (5 nm)/NiFe (4 nm) structure measured with magnetic fields along the x-axis (solid blue) and y-axis (open red). c,  $R_H$  versus azimuthal angle of a magnetic field ( $\phi_B$ ) of 100 mT. d, The  $R_H$  vs  $I_p$  curves, where the arrows denote the sweeping direction of  $I_p$ . e,  $R_H$  as a function of a magnetic field along x-axis ( $B_x$ ).  $R_H$  is initially set to  $\pm 0.14$  by an  $I_p$  of 30 mA, represented by the red and blue symbols. Open squares (lines) refer to increasing (decreasing)  $B_x$ . The inset illustrates the magnetization changes by  $B_x$ .

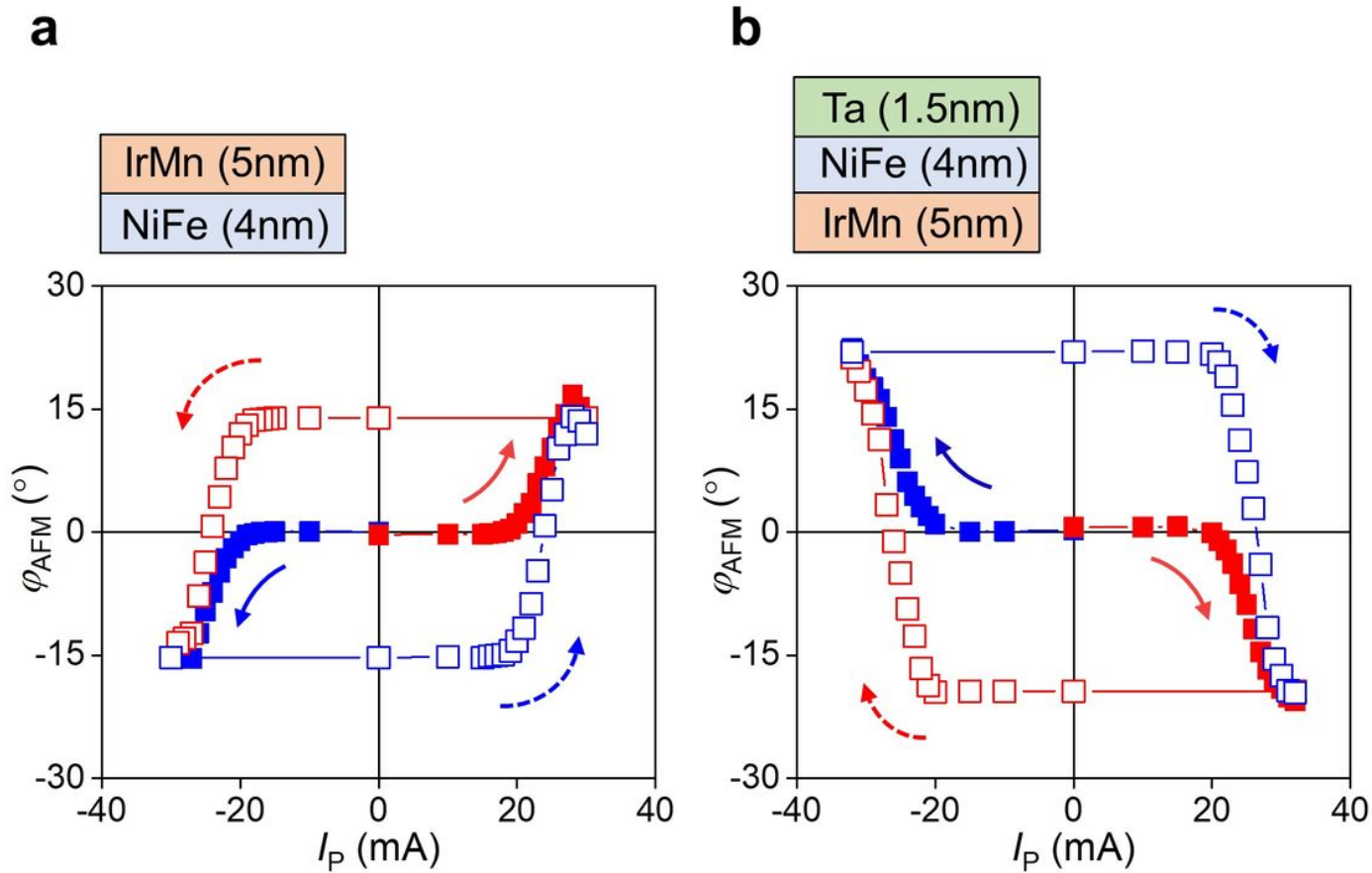


**Figure 2**

SOT-induced AFM switching for various IrMn/NiFe structures. a, b, AFM easy axis ( $\phi_{\text{AFM}}$ ) versus IP curves for the NiFe (4 nm)/IrMn (5 nm) sample (a) and the IrMn (5 nm)/NiFe (4 nm)/Ta (1.5 nm) sample (b). The arrows denote the sweeping direction of IP. The  $\phi_{\text{AFM}}$  values are extracted from the RH values.

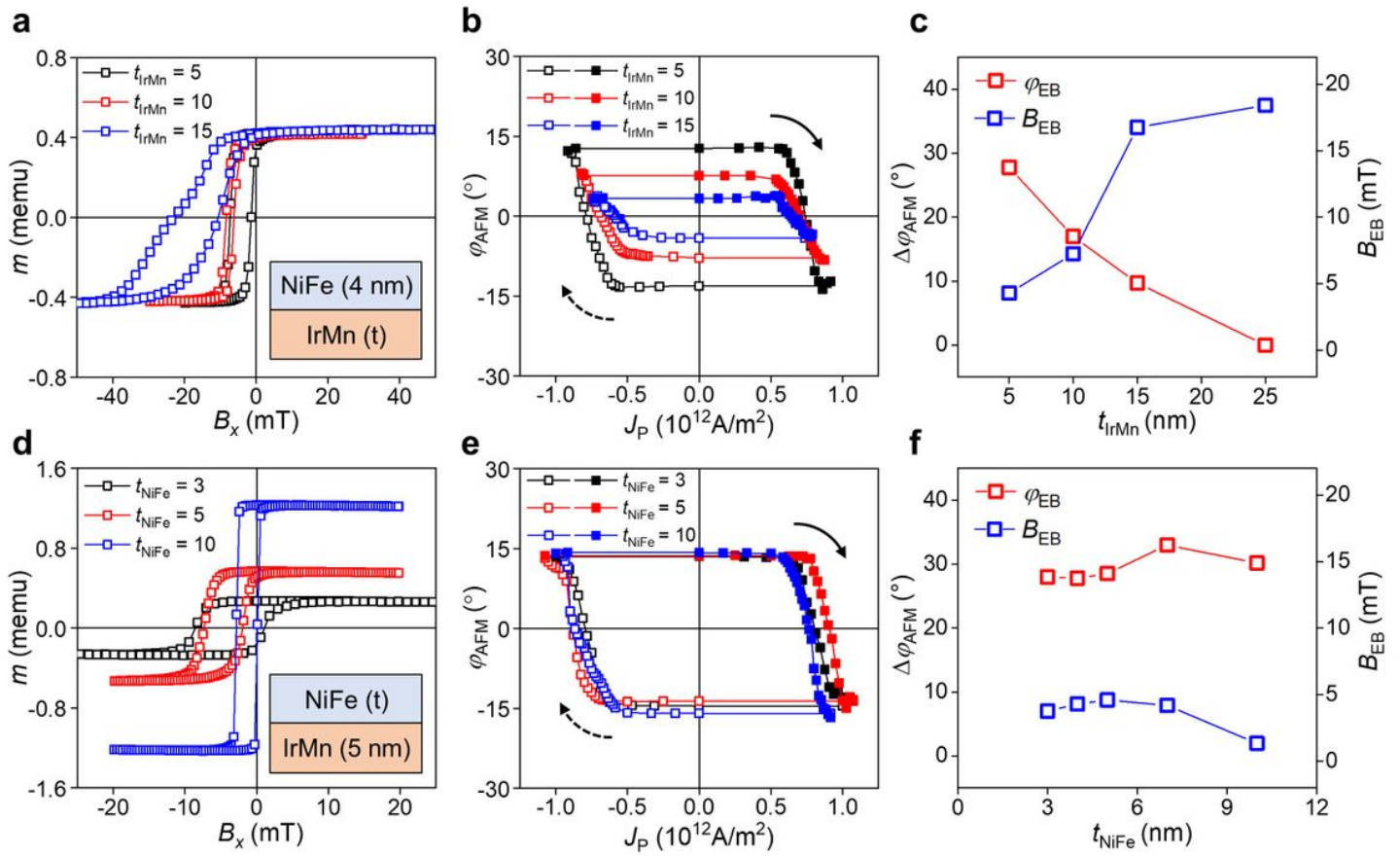


**Figure 3**

Thickness dependence of SOT-induced AFM switching. a-c. Hysteresis loop measured using a magnetic field along the x-axis,  $B_x$  (a), The  $\varphi_{\text{AFM}}$  versus current density ( $J_P$ ) curves, where the arrows denote the sweeping direction of  $J_P$  (b),  $\Delta\varphi_{\text{AFM}} [= j_{\text{AFM}}(-I) - j_{\text{AFM}}(+I)]$  and  $B_{\text{EB}}$  as a function of IrMn thickness  $t_{\text{IrMn}}$  (c) of the IrMn ( $t_{\text{IrMn}}$ )/NiFe (4 nm) samples with different  $t_{\text{IrMn}}$ 's ranging from 5 to 25 nm. d-f. Hysteresis loop measured using  $B_x$  (d), The  $\varphi_{\text{AFM}}$  versus  $J_P$  curves, where the arrows denote the sweeping direction of  $J_P$  (e), The  $\Delta\varphi_{\text{AFM}}$  and  $B_{\text{EB}}$  versus  $t_{\text{NiFe}}$  (f) of the IrMn (5 nm)/NiFe ( $t_{\text{NiFe}}$ ) samples with different  $t_{\text{NiFe}}$ 's ranging from 3 to 10 nm.

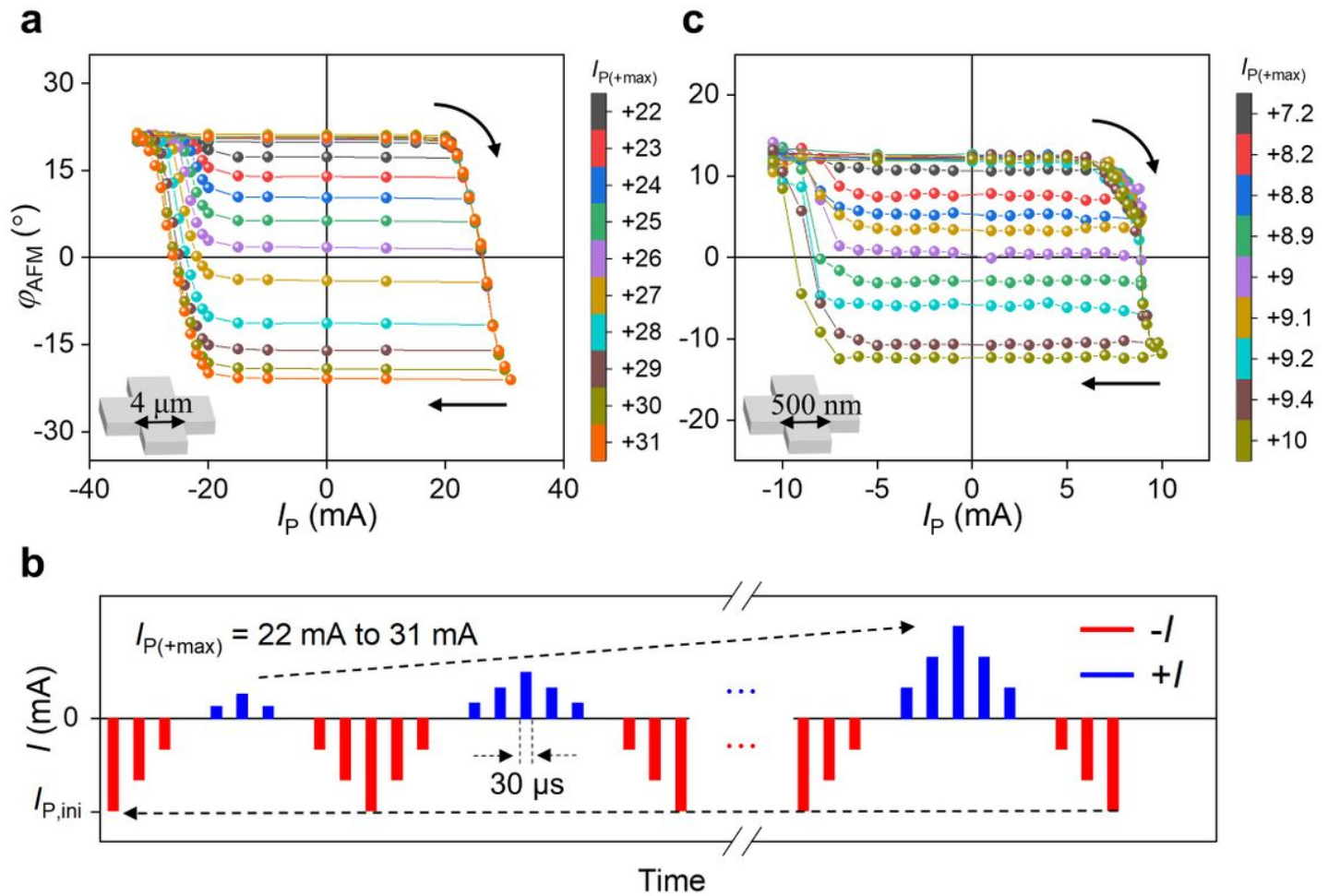


**Figure 4**

Memristive behaviour of AFM switching. a, Minor  $\phi_{\text{AFM}}$  vs  $I_P$  curves for the IrMn (5 nm)/NiFe (4 nm)/Ta (1.5 nm) sample with a 4- $\mu\text{m}$ -wide Hall bar. The arrows denote the sweeping direction of  $I_P$ , b, Schematics of the measurement sequence;  $I_{P,\text{ini}}$  is the initializing current pulse of -32 mA and  $I_{P(+\text{max})}$  is the positive maximum  $I_P$ . Minor loops are consecutively measured while sweeping  $I_P$  between -32 mA and  $I_{P(+\text{max})}$ , which increases from +22 mA to +31 mA. c, Minor  $\phi_{\text{AFM}}$  vs  $I_P$  curves for the IrMn (5 nm)/NiFe (5 nm) sample with a 500-nm-wide Hall bar. The arrows denote the sweeping direction of  $I_P$ .

## Supplementary Files

This is a list of supplementary files associated with this preprint. Click to download.

- [AFMSOTSINatComm.docx](#)